Discovering fiber type architecture over the entire muscle using data-driven analysis

Bindellini, D.; Voortman, L.M.; Olie, C.S.; Putten, M. van; Akker, E. van den; Raz, V.

TECHNICAL NOTE

Discovering fiber type architecture over the entire muscle using data-driven analysis

Davide Bindellini[1] | Lennard M. Voortman[2] | Cyriel S. Olie[1] | Maaike van Putten[1] | Erik van den Akker[3] | Vered Raz[1]

[1]Department of Human Genetics, Leiden University Medical Centre, Leiden, The Netherlands

[2]Department of Chemical Cell Biology, Leiden University Medical Centre, Leiden, The Netherlands

[3]Biomedical Data Science, Leiden University Medical Centre, Leiden, The Netherlands

Correspondence
Vered Raz, Department of Human Genetics, Leiden University Medical Centre, Leiden, Albinusdreef 2, 2333 ZA Leiden, The Netherlands.
Email: v.raz@lumc.nl

Funding information
AFM-Téléthon, Grant/Award Number: 26110; French Muscular Dystrophy Association

Abstract

Skeletal muscle function is inferred from the spatial arrangement of muscle fiber architecture, which corresponds to myofiber molecular and metabolic features. Myofiber features are often determined using immunofluorescence on a local sampling, typically obtained from a median region. This median region is assumed to represent the entire muscle. However, it remains largely unknown to what extent this local sampling represents the entire muscle. We present a pipeline to study the architecture of muscle fiber features over the entire muscle, including sectioning, staining, imaging to image quantification and data-driven analysis with Myofiber type were identified by the expression of myosin heavy chain (MyHC) isoforms, representing contraction properties. We reconstructed muscle architecture from consecutive cross-sections stained for laminin and MyHC isoforms. Examining the entire muscle using consecutive cross-sections is extremely laborious, we provide consideration to reduce the dataset without loosing spatial information. Data-driven analysis with over 150,000 myofibers showed spatial variations in myofiber geometric features, myofiber type, and the distribution of neuromuscular junctions over the entire muscle. We present a workflow to study histological changes over the entire muscle using high-throughput imaging, image quantification, and data-driven analysis. Our results suggest that asymmetric spatial distribution of these features over the entire muscle could impact muscle function. Therefore, instead of a single sampling from a median region, representative regions covering the entire muscle should be investigated in future studies.

KEYWORDS
data-driven analysis, muscle architecture, myofiber type, quantitative image analysis

1 | INTRODUCTION

Skeletal muscles facilitate the mobilization and stability of the skeleton, which is greatly determined by muscle fiber architecture. Muscle function changes in physiological, pathological conditions, and during development [1, 2]. Muscle fiber spatial arrangement is broadly described by their orientation relative to the axis of force generation, which can be classified into three main classes: 1) fibers arrangement

parallel to the force-generating axis on both ends of the muscle. 2) fiber orientation at a single angle relative to the force-generating axis. 3) multiple fiber orientation relative to the axis of force generation [3–5]. Muscle fibers are often characterized using histological features, such as cross-sectional area, metabolic features, molecular signatures, and molecular networks [6–8].

Contraction properties are also determined by myofiber types, which can be grouped to fast- or slow- twitch fibers [9, 10]. Fast- or slow-twitch fibers are marked by the expression of different myosin heavy chain (MyHC) isoforms [9]. In mice, the fast-twitch muscle fibers express MyHC-2A, -2B isoforms, and slow-twitch express MyHC-1. The MyHC-2B type muscle fibers produce energy by glycolysis, whereas the MyHC-2A fibers use fatty acids for energy production [9]. In mice, specific muscles are defined as fast muscles, like tibialis anterior (TA) or Extensor digitorum longus (EDL), as both contain mainly fast twitch fibers. In contrast, in slow muscles, like soleus, fibers express mainly MyHC-1 and MyHC-2A [9, 10]. Alterations in MyHC isoform expression occur in physiological conditions like training or aging, and in pathological conditions [11, 12]. Understanding alterations in myofiber typing (transitions) in different conditions should employ data-driven (unbiased) analysis of individual myofibers, requiring large myofiber dataset(s). Most often, the expression of MyHC isoforms is determined from a single median cross-section. It is unsettled whether a median sampling represents the entire muscle.

Methods to identify myofiber types using an antibody mix containing fluorescently conjugated anti MyHC isoforms have been developed [13, 14]. Using this antibody mix, procedures to quantify myofiber type together with high-throughput imaging and myofiber quantification procedures resulted in large myofiber datasets, from which myofiber composition and the spatial arrangement could be studied using data-driven analyses [7, 15, 16]. Data-driven analysis can further improve the understanding of myofiber transitions in disease and physiological conditions [16–18]. Those studies on myofiber composition and changes in disease animal models are most often carried out in cross-sections taken from a median region of the muscle. It has been reported that the expression of the MyHC isoforms varies over the longitudinal axis of myofibers [19]. Yet, the spatial organization of myofiber type over the entire muscle is not fully understood.

A simulation of muscle movement using architectural models, suggested that even in a muscle with a parallel muscle fiber arrangement, like the TA, the contraction is not symmetric over the muscle longitudinal axis [3, 20–22]. The TA connects the knee to the foot, mobilizing the lower leg [23]. Modeling of myofiber architecture from noninvasive imaging procedures also reported asymmetric myofiber organization over the TA longitudinal [24, 25]. These reports demonstrate the importance of the analysis of myofibers over the entire muscle. However, they do not discriminate between fiber types within the muscle.

Here we present a workflow to investigate myofiber type arrangement over the entire muscle using myofiber data-driven analysis and discuss the critical steps in this procedure. Based on our pilot study we suggest that a functional analysis of the muscle should not be based on single cross-sections.

2 | METHODS

2.1 | Animals

Eight-weeks-old male C57BL/6J wild-type mice were cultivated in the same cage and were sacrificed by cervical dislocation after CO_2 euthanasia. The TA muscles were collected from the same nest and mice that grew in the same cage, and immediately snap-frozen in liquid nitrogen in the presence of iso-pentane and were stored at $-80°C$, as described in [16, 17]. Only the right TA muscles from two mice were used in this study. Experiments in mice were approved by the Animal Experiment Committee (DEC 13211) of the Leiden University Medical Centre.

2.2 | Sectioning and immunofluorescence

One muscle was sectioned in a transverse axis from one end to the other, and the other muscle was sectioned in a longitudinal axis. For cross sections, the muscle was mounted at the distal side, therefore the distal end was excluded from the cross sections. The sections' numbering starts from the distal side and the first section is noted as 0 μm. Ten micrometer thick sections were pasted on superfrost slides. For each staining, at least three longitudinal sections were used. In total, 603 transverse sections covered the entire muscle. The tips at the distal or proximal ends were excluded, as those could not be sectioned. Sections were made with the CM3050-S cryostat (Leica Germany), and were pasted on "PTFE" printed slides, 12 well—5 mm diameter, (Electron Microscopy Sciences, USA). Sectioning of the entire muscle was carried out in a single day without removing the muscle from the cryotome. This eliminates differences in the cutting angle (tissue orientation, which will affect myofiber geometry) and batch effect. Muscle sections were stored at $-20°C$ before staining.

The immunohistochemical procedure was performed with a staining protocol that is detailed in [16]. Sections were stretched in a PBS solution before the immunofluorescence procedure. The antibody mix contained the fluorescently conjugated compounds: antibodies to MyHC-2B_Alexa fluor-488-conjugated (1:400), MyHC-2A_Alexa fluor-594-conjugated (1:1000) (homemade [18]), and rabbit-anti-Laminin (1:1000, Abcam, UK) visualized with Goat-anti-Rabbit_Alexa-647 (1:1000, Life Technologies, USA). The α-Bungarotoxin_Alexa fluor-488-conjugated (1:1000) was purchased from Thermo Fisher and it was used to stain the neuromuscular junction (NMJ). Cross-sections were stained using the MyHCs antibody mix. Slides were mounted with ProLong Gold (Invitrogen, USA). All cross-sections were stained using the same antibody mix in a single batch to eliminate variations between staining sessions. The length of the

entire muscle or an individual muscle fiber were measured from longitudinal sections using the microscope scale bar.

2.3 | Imaging

Imaging was performed with the Pannoramic 250 Flash II slide scanner (3DHISTECH, Hungary). Imaging of all cross-sections was carried out in a single session, eliminating batch effects. Imaging of the α-Bungarotoxin signal was performed with both the slide scanner and a higher resolution with the Leica DM5500. The α-Bungarotoxin staining of the NMJs were recognized and manually counted from the high-resolution images. Counting was carried out by two observers. NMJ counts per observer are found in Table S1.

2.4 | Image processing, quantification, and alignment

Slide scanner images were stitched, and files were converted to TIFF using CaseViewer (3DHISTECH, Hungary). After conversion, images were cropped and scaled using custom MatLab (MathWorks Inc.) scripts. Scaling of the images (4x down-sampling by averaging, to an effective pixel-size of 1.3 μm) was possible because sufficient details were retained while simultaneously increasing the processing speed. The size of the cropped and scaled section depended on the section's size. After segmentation, the size of images was uniform for all sections: 3456 x 2560 pixels.

The TIFF images were processed and subsequently, the laminin was segmented. Quantification of the cross-sectional area (CSA), circularity and spatial position were made from the lamina segmentation. In addition, per myofiber, the mean fluorescence intensity (MFI) of MyHC-2B and MyHC-2A were measured. This analysis was carried out using parts of the MuscleJ V1_0_2 [15] macro combined with custom macros in ImageJ V1.52k. From the original MuscleJ, only the myofiber segmentation was used. We applied the following modifications to the original MuscleJ: the image processing step (before segmentation) was changed to match our image resolution (e.g., operations that are based on the number of pixels instead of a physical size were tweaked to improve the segmentation). Subsequent quantification of MFI, circularity, and spatial position (x, y coordinated) was performed using an ImageJ macro that reads the segmentations from MuscleJ (an example of tissue outcome after segmentation is shown in Figure S1). The output file included: section number, position, myofiber number, CSA, circularity, spatial position, MyHC-2B and MyHC-2A MFI. The modified macros can be obtained upon request. We noticed that these uniform image processing and segmentation settings were not optimal for all sections, but we compromised for a uniform procedure over manual optimization for every section.

We then excluded sections due to technical issues (folded, broken, mounting; examples are in Figure S2; 453 sections), and due to bad segmentation (21 sections). Based on the MyHC-2A length

(160 μm or longer), we aimed for a 150 μm or less gap between consecutive images. Segmentation was verified after a visual assessment of lamina segmentation in comparison with the original image. In total, 129 sections that were evenly distributed along the muscle, were used for analysis. The impact of the excluded sections on subsequent analyses was assessed using an alignment of the sections. The alignment of the images was performed in ImageJ using Linear Stack Alignment with the scale-invariant feature transformation (SIFT) algorithm [26]. This method aligns sections consecutively one after the other requiring a maximum similarity between consecutive sections. Sections were mapped to their physical position over the muscle longitudinal axis. Sections' position was calculated with the first section at zero μm and consecutively increasing by 10 μm (sections thickness), including the position of the excluded sections. To improve the alignment type-2A positive objects were defined with a "2A-mask" under an arbitrary statistical definition (MFI was greater than mean MFI + SD) per section.

Median and variance for both CSA and circularity were calculated per section. MyHC MFI was obtained per myofiber object, and although staining was carried out in a single day, and imaging was also carried out in a single batch, we observed differences in the background MFI between sections. Therefore, background correction was separately applied to each image and fluorophore by subtracting the MFI measured from a region without the tissue followed by natural logarithm (ln) transformation of MFI values, as described in [7]. As technical differences between images could still be observed after background correction, MFI values were scaled per section by using the "scale" function in R with default settings. Myofiber MFI analysis was carried out using R (version 3.5.1). Smoothing regression lines were calculated and plotted using the smooth. spline function in R, using smoothing parameter = 1. The smooth regression line levels off small variations between adjunct cross-sections.

The muscle area for normalization of NMJ counts was segmented and measured in ImageJ using the lamina staining. The muscle regions were made using the muscle region proportions that were made from the cross-sectional study.

3 | RESULTS

3.1 | Wet-lab and imaging workflow

To study muscle fiber features over the entire muscle we developed a high-throughput and data-driven methodology using the TA muscle. The TA size is small enough to complete the wet-lab workflow in a single batch, avoiding a batch effect. The methodology workflow is summarized in Figure 1. One muscle was cross sectioned from the distal to the proximal end, and the other one was sectioned on the longitudinal axis (Figure 2(A)). The entire muscle length and myofibers' length were measured from the median longitudinal sections. Our TA muscles were around 6 mm prior to and after sectioning (Figure 2(B,C)). The TA length is in agreement with a previous report [27]. Image processing and quantification were carried out on the cross-sections, and data-driven
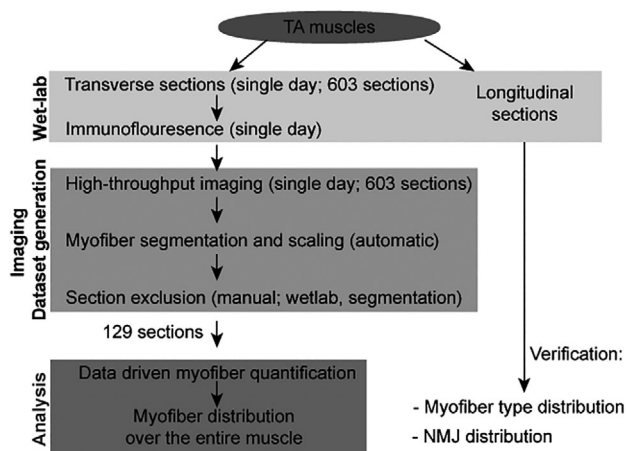
FIGURE 1 A methodological summary of myofiber data collection and analysis. The workflow of the transverse sections is shown on the left side: wet-lab procedures, imaging, image processing, segmentation, and scaling and tissue exclusion are all categorized as dataset generation. Data-driven analysis of myofiber features over the entire muscle. The asymmetric distribution of myofibers and expression of markers were verified in the longitudinal sections

analyses were carried out on data generated from the cross-sections. The longitudinal sections were used as a reference and for verifications of results from the cross-sections. A schematic representation of the TA anatomy is shown in Figure 2(A).

Throughout the entire muscle, muscle fibers positive to MyHC-2B were more prominent compared with MyHC-2A, and some MyHC-2B myofibers encompassed the entire muscle length (Figure 2(C)). The length of MyHC-2A myofibers was estimated from three longitudinal sections at a median region of the muscle (ranged between 160–250 μm). Technical issues in the wet-lab procedure included tissue break, tissue folding and uneven mounting (Figure S2), which resulted in insufficient segmentation. We excluded sections with segmentation 30% or less of the section area. After section exclusion, the maximum gap between two sections included in the analysis was found as 140 μm. With this gap size we ensure not missing any MyHC-2A myofibers in the dataset. In addition, to avoid an over-representation in certain regions, we retrospectively ensured that the sections were evenly distributed over the entire muscle. After the exclusion, 129 sections remained for subsequent analysis.

## 3.2 | Assessment of sections' exclusion using myofiber alignments

To assess the impact of the excluded sections on subsequent analyses we investigated myofiber alignment across sections. The SIFT based alignment results were two: either a failure in the identification of any correspondence between sections, that resulted in an output that did not preserve myofibers' architecture (wrong alignment), or an alignment output that preserved myofiber architecture, which was in close

agreement with an eye-based alignment. Using both laminin segmentation and the *2A-mask*, marking the 2A-positive fibers, improved the alignment output (Figure 2(E)). Myofibers' alignment was also visually assessed (examples are in Figure 3). An alignment was obtained for both an image set of sequential sections and an image set of gaps between sections over the same area (Video AVI S1 and S2, respectively). Based on visualization, the two alignments were comparable, meaning that no failures were observed. This suggests that exclusion of sequential sections, under the criteria that the gap size is equal or less than the smallest fiber length, would maintain myofiber spatial information.

To further assess this, we then extended the alignment to other muscle area. An alignment over the entire muscle was not possible, as the alignment is hampered by the accumulation of errors over sets of sections. Thus, technical wet-lab issues, like tissue breaks, hampers the alignment. Therefore, we performed local alignment for sections at the distal, median and proximal regions, and similar gaps between sections allows a visual comparison (Figure 3). Overall, an overlap across myofibers was visually clearer in both median and proximal regions of the muscle, compared with the distal side of the muscle (Figure 3(B)). The overlap between 2A-positive fibers appears to be more prominent at the proximal region (Figure 3(B)).

## 3.3 | The distribution of myofiber features over the entire muscle

The change in myofiber alignment over the longitudinal axis suggests that myofiber properties might alter over the entire muscle. In total, 153,930 objects from 129 cross-sections were included in the analysis. From the laminin segmentation we extracted CSA and circularity. As the entire muscle was sectioned in a single session, the same cutting angle was kept over the entire muscle, therefore a change in CSA or circularity could not reflect alterations in sectioning orientation but instead a biological phenomenon. We plotted the median CSA, median circularity, and the variance of both features per section and applied a smoothed regression line (curved) to show the change along the muscle (Figure 4(A–E)). The smoothed regression line enables to describe major changes over the longitudinal axis while disregarding the effect of an individual cross-section or a small group of consecutive sections. The shape of the regression line for the number of myofibers follows the macro shape of the TA muscle: smaller at the distal region, larger at the median region, and getting smaller at the proximal region (Figure 4(A,B)). The regression line describing the change in myofiber number over the muscle was not affected by nine consecutive sections, at position ~3000–3500 μm, having nearly half of myofibers compared with the environs sections (Figure 4(A,B)). Using the median CSA, two regions could be discriminated: the distal region had myofibers with smaller CSA compared with the other side of the muscle (Figure 4(C)). The regression line of the median circularity and the variance of circularity showed an opposite trend over the entire muscle (Figure 4(D)). Using the intersection between the median circularity and the circularity variance regression lines we defined the distal region (Figure 4(D)). High circularity values indicate
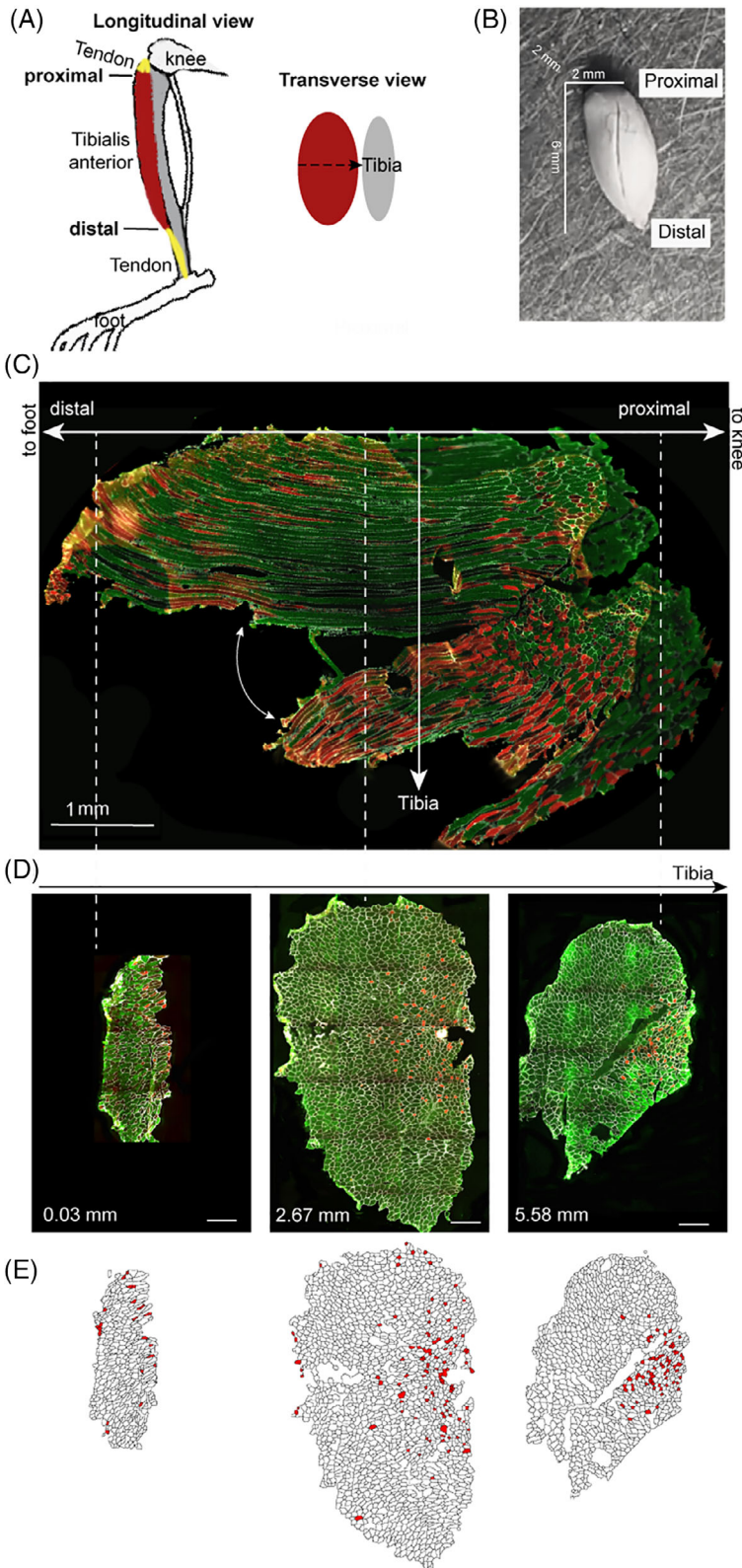
FIGURE 2 A summary of tibialis anterior imaging. (A) A schematic representation of the TA anatomy in longitudinal and transverse views. The tibia is depicted in dark gray, the TA muscle in dark red, and the tendon in yellow. (B) An image of a TA muscle before sectioning. Proximal and distal ends are denoted. (C,D) Representative stitched images from longitudinal (C) and cross-sectional sections (D) immunofluorescence staining with MyHC-2B (green), MyHC-2A (red), and laminin (white). Muscle positions are denoted. Dashed white lines show corresponding positions between the longitudinal and the cross-sections. The curved white arrow in C depicts the area that detached during sectioning. The scale bars are 1000 μm. (E) Images show segmentation of the stained images in (D). Fiber segmentation is in black lines and the 2A-positive fibers are in red [Color figure can be viewed at wileyonlinelibrary.com]

circle myofibers whereas low values indicate elongated orientation. High variance indicates heterogeneity. To assess a spatial relation between CSA and circularity, we combined the median CSA and median circularity regression lines, and then further defined muscle regions in this TA muscle (Figure 4(E)). The four regions are (Figure 4(F)):

the distal region (r1) (~1/11 of the muscle) myofibers CSA is small and circularity is low with high variance indicating heterogeneity in myofiber structure. In r1/2 (~1/5th of the muscle) myofibers are more circular but their CSA remains small. In the median part, r2 ~ 2/3rd of the muscle, myofibers have both high CSA and circularity values, and the small
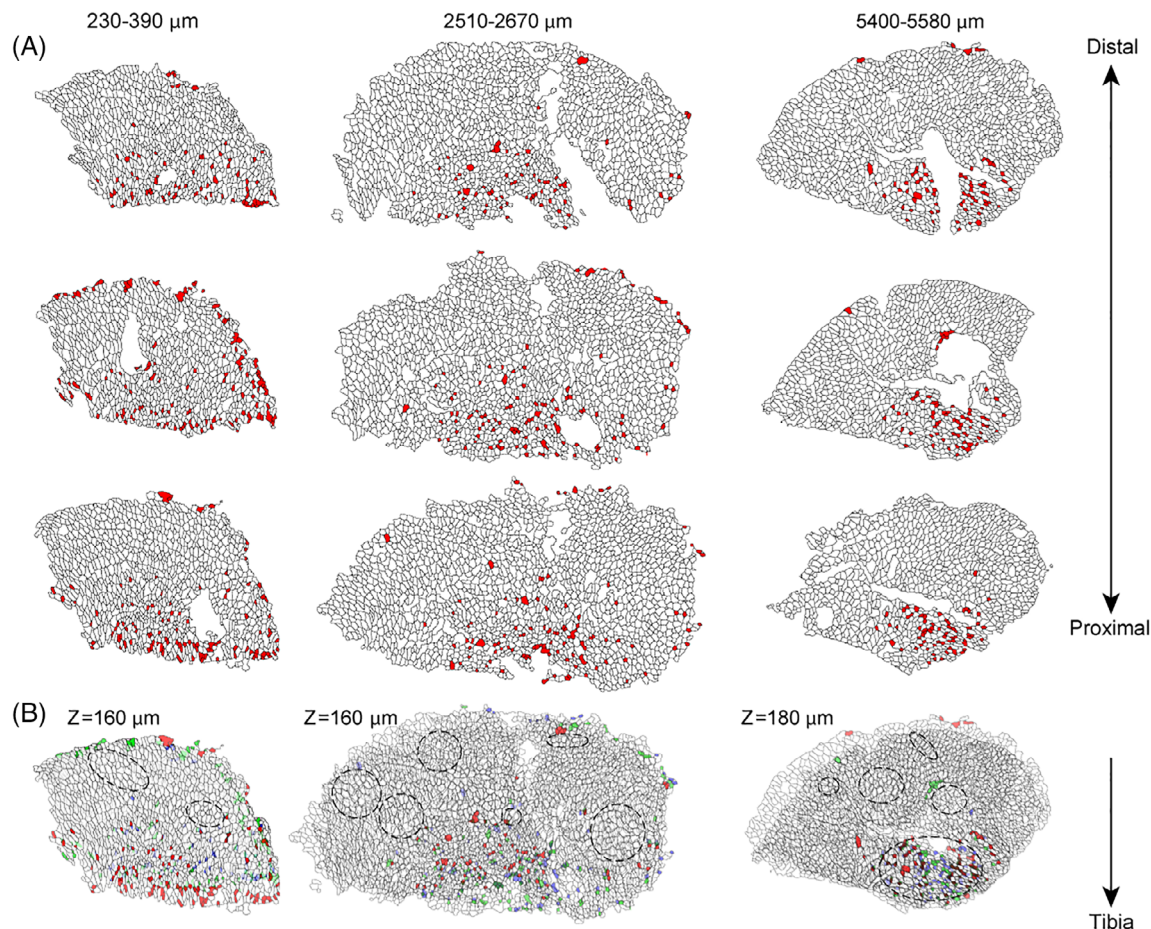
FIGURE 3 Alignment overlay of three cross-sections in three muscle regions. (A) Images of individual muscle cross-sections after fiber segmentation. (B) the alignment overlay results. The distal–proximal axis in (A) is across the three sections. The side facing the tibia is depicted in (B). In the overlay image, myofibers in red, green or blue, mark the 2A-positive fibers in the distal, middle or proximal section, respectively. Overlap of lamina segmentation is seen with a higher intensity and overlapping 2A-positibe fibers are brown. Examples of regions with overlapping myofibers are encircled with a dashed line. Positions of the sections over the longitudinal axis and depth of every three sections (Z) are denoted [Color figure can be viewed at wileyonlinelibrary.com]

variance in circularity suggests a more homogenous structure of fibers. At the proximal region, the smallest regions, (r3; ~1/20th of the muscle), the median circularity decreased while the median CSA increased (Figure 4(F)).

To assess the robustness of this analysis, we compared the regression line for CSA and circularity between the dataset made from 129 sections and a dataset from 71 sections. To create this sub-dataset, only the sections with and "odd" position were kept. The regression lines of the two datasets nearly similar for the median CSA and circularity (Figure S3). This indicates the analysis of median CSA or circularity is robust and allows gaps larger than 140 μm between sections.

We then investigated if the muscle regions, as defined by geometrical features of the myofibers, can be distinguished by molecular features, such as myofiber type. The main myofiber-type expressing MyHC-2B or MyHC-2A subclasses were determined in the pooled dataset. The MyHC-2B density plot showed only a single peak, but two peaks were found in the MyHC-2A density plot (Figure 5(A)). This

indicates that in TA, the MyHC-2B myofibers form a homogenous population, but the MyHC-2A myofibers can be categorized into two groups, one with high and one with low expression levels. For a spatial assessment of myofiber type over the entire muscle, we focused on the 2A-positve myofibers (Figure 5(A)). We distinguished between the 2A-positive myofibers and the 2A-negative myofibers using density distribution of MyHC-2A MFI, and then calculated the percentage of type-2A positive myofibers in every section. An overlay of the percentage of 2A-positive myofiber and the median CSA showed that in general, in sections with a high percentage of 2A-positive myofiber, the median CSA was small and vice versa (Figure S4), which is in agreement with our previous data-driven analysis in human muscles [7]. The proportions of type-2A positive myofibers from the myofibers per region were in r1 and r1/2 nearly two-fold higher compared with r2 and r3 (Figure 5(C)). This indicates an uneven distribution of type-2A myofibers along the TA muscle. The distribution of the 2A-positve myofibers along the muscle was affected in the reduced dataset, with gaps larger than 140 μm (N = 71 sections; Figure S3). This indicates
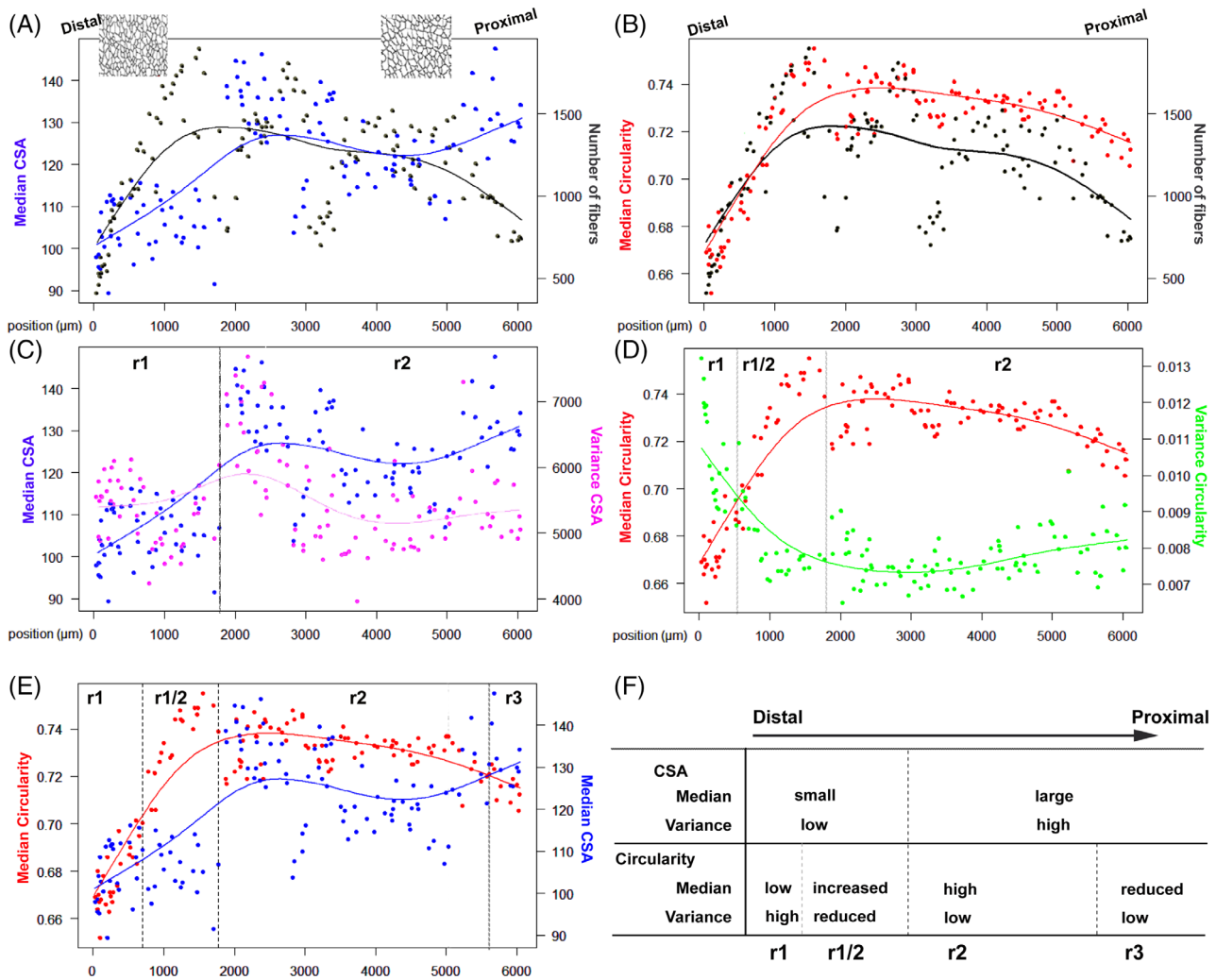
FIGURE 4 Analysis of muscle fiber features over the TA muscle. (A–E) Scatter plots of fiber measurers: CSA (blue) and circularity (red). In (A,B) median CSA or median circularity are plotted together with the number of fibers. Every dot represents a single cross-section. The variance of CSA or circularity is depicted in pink or green, respectively. Cross-sections are positioned in chronological order from distal to proximal ends (x-axis, in μm). The smoothed regression lines (curved lines) show major changes over the muscle. Dashed lines mark regions defined by the regression lines. Regions (r) 1 and 2 are defined by the median CSA (C). The r1 is split into r1 and r1/2 based on circularity (D). The r3 is further defined by both CSA and circularity (E). (F) A summary of region definition using CSA and circularity [Color figure can be viewed at wileyonlinelibrary.com]

that the reduced dataset was not beneficial to analyze the distribution of the 2A-positive myofibers.

Last, we assessed the distribution of NMJs over the TA in longitudinal sections from the second muscle (Figure 5(B)). The NMJs were visualized with an antibody to α-bungarotoxin, which specifically binds to NMJs [28] and were manually detected. As the length of the two TA muscles was similar, we estimated the location of the four regions from the cross-sectional study (Figures 4(E) and 5(A)) using the scale bar. The distribution of NMJs along the muscle was found to be uneven, the lowest NMJ proportions were found at the distal end, and the majority of NMJs were found at the median region (Figure 5(C) and Table S1).

4 | DISCUSSION

It has been recognized that we are still far from understanding how myofiber histological features affect contraction and the specific movement function [29]. The impact of myofiber type on muscle physiology and function has been mostly interpreted from cross-sections at the median part of the muscle. Several reports reinforced that for understanding how myofiber architecture affects muscle function it is important to sample over the entire muscle [22, 30]. In agreement with those studies, we suggest that muscle function cannot be drawn from a single (median) cross-section. In contrast to previous studies [22, 27, 30–32], we also considered the spatial
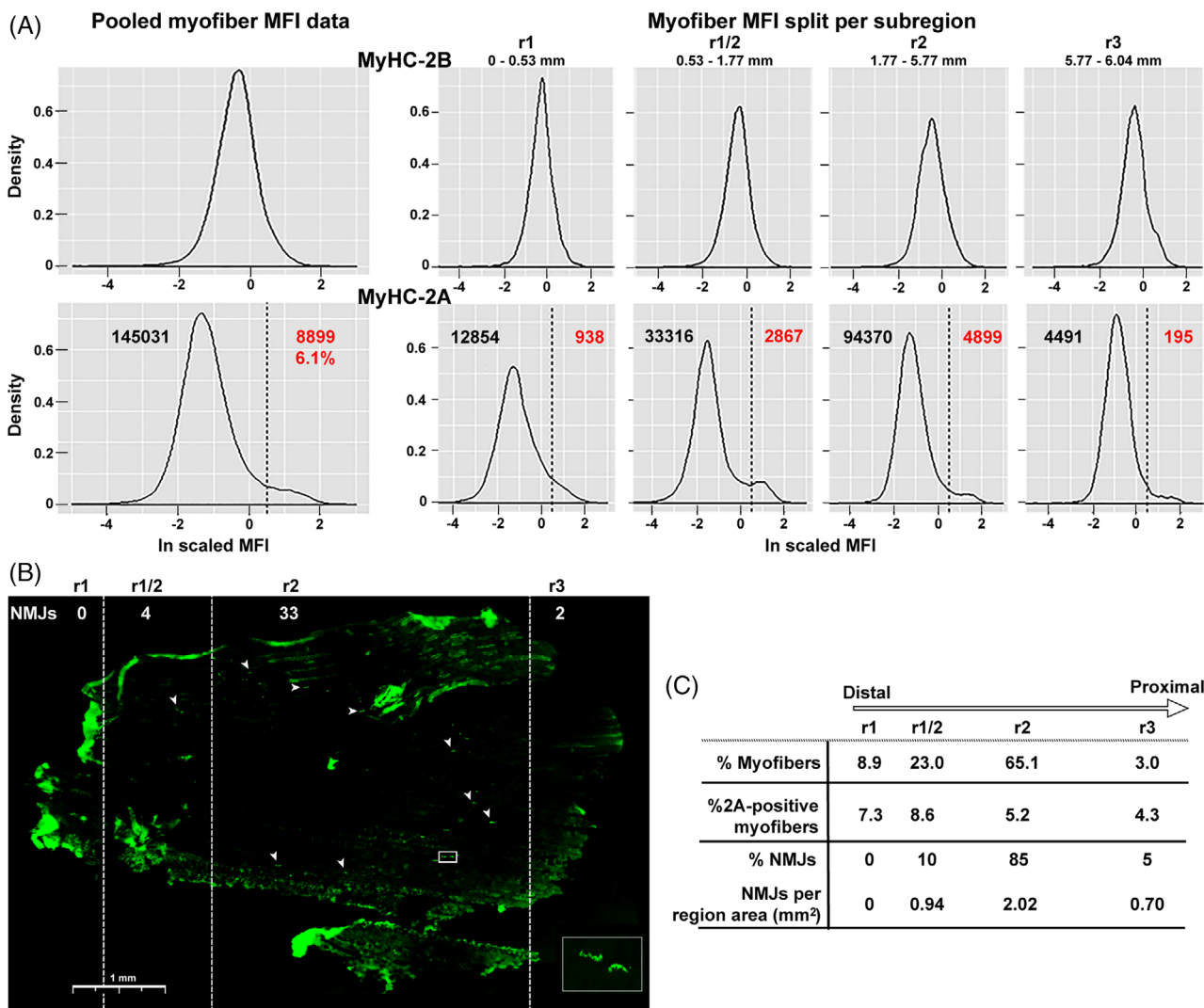
FIGURE 5 Analysis of muscle fiber type and NMJs over the TA muscle. (A) Density plot of MyHC-2B (upper row) and MyHC 2A (lower row) mean fluorescence intensity (MFI) in the pooled data (combined sections) or per region (r1, r1/2, r2, r3, as defined in Figure 4(E)). Positive and negative fibers are defined by the MFI distribution in the pooled data, and the same threshold, depicted with a dashed line, was used for all regions. The number of 2A-negative or positive fibers are depicted in black or red, respectively in each plot. The range of each region (in mm) is indicated above the plots. (B) A representative immunofluorescence image of a longitudinal section stained with Alexa-488-conjugated α-bungarotoxin, marking NMJs. An example of NMJs obtained with a 20X objective is depicted in the white rectangle. Examples of NMJs are depicted with an arrowhead. The estimated regions are depicted with dotted lines. The area of the regions was calculated in proportion to the regions in A. The average NMJs (rounded numbers) per region is depicted. The scale bar is 1 mm. Dashed lines mark the estimated muscle regions. (C) A summary of the % of myofibers per region, the % of 2A-positive fibers, NMJs percentage from the total counts, and the number of NMJs corrected to the region area (mm^2) [Color figure can be viewed at wileyonlinelibrary.com]

organization of myofiber types over the entire muscle. Our methodological paper, therefore, also reinforces the importance of adequate spatial sampling of whole muscles in future studies.

Modeling muscle fiber architecture has been studied using non-invasive methods and ex-vivo imaging procedures. For the TA, a parallel myofiber arrangement has been reported, where most fibers are parallel to the longitudinal axis at the largest part of the muscle but close to the tendon at the distal end, myofibers curve [21, 27, 33]. This indicates an asymmetric myofiber architecture over the entire muscle. Asymmetric distribution of myofiber types over the entire muscle was also previously reported [34], but this is the first

study combining immunofluorescence of MyHC isoforms and data-driven analysis. The asymmetric distribution of 2A-positive myofibers and NMJs over the longitudinal axis suggests that contraction properties are not uniform throughout the muscle. This emphasizes that a single sampling of the muscle at the median region is not sufficient.

Myofiber typing is carried out by either ATPase staining or MyHC immunofluorescence. The ATPase staining is simpler, cheaper and faster. MyHC isoforms' expression in myofibers can lead to better understanding of myofiber type organization in muscles [7, 18]. An asymmetric distribution of slow-twitch myofibers was reported in limb muscles using ATPase staining [34]. Here, we report an asymmetric

distribution of the 2A-positive myofibers, which were found to be more abundant at the proximal side of the TA muscle. This could suggest differences in contraction properties along the muscle.

Ex-vivo measurements of sarcomere force-length demonstrated that myofiber architecture affects its biomechanical properties [22]. Ex-vivo procedures of muscle architecture can influence the shape of the muscle during the following procedures: 1) Pulling when dissecting the muscle out of the mouse. We were careful avoiding pulling tissue. Yet, pulling could have an impact comparing different muscles. 2) The natural muscle-tendon tension affecting muscle length, cannot be considered in this ex-vivo study. In principle, a fast muscle freezing, immediately after harvesting, should limit tension and length loss during muscle harvesting. Freezing artifacts could also contribute to variations between muscles. 3) Mounting could affect myofiber orientation. Therefore, in our workflow sectioning of the entire muscle was carried out in a single day, without dismounting of the muscle from the cryotome, and the section angle relative to the muscle axis was identical across all sections. Despite these issues that could affect muscle architecture, our observations from the ex-vivo analyses of myofiber organization are in agreement with results obtained from intact muscles. We also found asymmetric myofiber arrangement over the longitudinal axis. At the distal region, myofibers had small CSA and showed heterogeneity of circularity suggesting that part of the myofibers bend. This supports the distal region lanceolate shape. Ideally, an ex-vivo study of myofiber architecture would be performed in sections of an entire lower leg, in which a muscle is connected to the bone(s) and other tissues exactly as in the full organism. This approach could be investigated in future studies, making use of the workflow we are reporting here.

Analytical two-dimensional skeletal muscle models predicted that the shape of myofibers affects intramuscular pressure distribution [35]. Other models suggest that pressure distribution over the muscle is not even, the high-pressure region presents half-way over the muscle length, which supports the bending of the myofibers [20]. At the median region, we found that both CSA and circularity have the largest range. This could indicate that the geometry of those myofibers supports high pressure. Compared with the median region, at the proximal end, the CSA had higher values compared with circularity. This could indicate that the proximal end of the TA is a vulnerable area for muscle pressure. The observed asymmetry of geometrical features of myofibers over the entire muscle is consistent with biomechanical models of the TA muscle [21, 27, 33]. Moo et al., also measured sarcomere force at the median region of a muscle and stressed that their findings may not be valid to other muscle regions, especially where myofiber lengths are not uniform [22].

Under the assumption that we aim to describe major changes over the muscle, we applied a smoothed regression line to describe changes in myofiber features over the muscle. Therefore, small sub-regions, consisting of only a few sections, were not considered. Combining the regression lines of median CSA, median, and variance circularity we described four muscle regions. We suggest that these regions could have different muscle functions based on myofiber type and the NMJs counts. Myofiber type and NMJs

density affect contraction [36]. This pilot study was carried out on one muscle and specific conclusions as to regions function should be cautiously made.

In this methodological paper, we describe a workflow to investigate myofibers' features over the entire muscle. In this study, we focused on geometrical features, myofiber type, and NMJs. We show that the number of sections can be reduced without affecting spatial information. Combining image quantification with data-driven analysis spatial information can be collected and myofiber patterning over the muscle could be recognized. When applied to varied physiological and pathological conditions, this methodology has the potential to report changes in myofiber features over the entire muscle and could indicate changes in muscle function. Additionally, different staining could be performed on alternating sections, increasing the number of features studied over the entire muscle.

ORCID

Vered Raz https://orcid.org/0000-0003-3152-1952

REFERENCES

1. Siebert T, Tomalka A, Stutzig N, Leichsenring K, Böl M. Changes in three-dimensional muscle structure of rabbit gastrocnemius, flexor digitorum longus, and tibialis anterior during growth. J Mech Behav Biomed Mater. 2017;74:507–19.
2. Siparsky PN, Kirkendall DT, Garrett WE Jr. Muscle changes in aging: understanding sarcopenia. Sports Health. 2014;6:36–40. https://doi.org/10.1177/1941738113502296
3. Otten E. Concepts and models of functional architecture in skeletal muscle. Exerc Sport Sci Rev. 1988;16:89–137.
4. Lieber Richard L, Ward SR. Skeletal muscle design to meet functional demands. Philos Trans R Soc B. 2011;366:1466–76. https://doi.org/10.1098/rstb.2010.0316
5. Lieber RL, Fridén J. Functional and clinical significance of skeletal muscle architecture. Muscle Nerve. 2000;23:1647–66. https://doi.org/10.1002/1097-4598(200011)23:11<1647::aid-mus1>3.0.co;2-m
6. Frontera WR, Ochala J. Skeletal muscle: a brief review of structure and function. Calcif Tissue Int. 2015;96:183–95.
7. Raz Y, van den Akker E, Roest T, Riaz M, van de Rest O, Suchiman H, Lakenberg N, Stassen S, van Putten M, Feskens E and others. A data-driven methodology reveals novel myofiber clusters in older human muscles. FASEB J 2020;34:5525–37. https://doi.org/10.1096/fj.201902350r
8. Chemello F, Bean C, Cancellara P, Laveder P, Reggiani C, Lanfranchi G. Microgenomic analysis in skeletal muscle: expression signatures of individual fast and slow myofibers. PloS One. 2011;6:e16807.
9. Schiaffino S, Reggiani C. Fiber types in mammalian skeletal muscles. Physiol Rev. 2011;91:1447–531.
10. Lang F, Khaghani S, Türk C, Wiederstein JL, Hölper S, Piller T, et al. Single muscle fiber proteomics reveals distinct protein changes in slow and fast fibers during muscle atrophy. J Proteome Res. 2018;17:3333–47.
11. Pette D, Staron RS. Myosin isoforms, muscle fiber types, and transitions. Microsc Res Tech. 2000;50:500–9.

12. Baskin KK, Winders BR, Olson EN. Muscle as a "mediator" of systemic metabolism. Cell Metab. 2015;21:237–48.

13. Bloemberg D, Quadrilatero J. Rapid determination of myosin heavy chain expression in rat, mouse, and human skeletal muscle using multicolor immunofluorescence analysis. PloS One. 2012;7:e35273.

14. Kammoun M, Cassar-Malek I, Meunier B, Picard B. A simplified immunohistochemical classification of skeletal muscle fibres in mouse. Eur Histochem. 2014;58:2254–4.

15. Mayeuf-Louchart A, Hardy D, Thorel Q, Roux P, Gueniot L, Briand D, et al. MuscleJ: a high-content analysis method to study skeletal muscle with a new. Skeletal Muscle. 2018;8:25.

16. Raz V, Raz Y, Dvd V, Bindellini D, Mv P, EBvd A. High-throughput data-driven analysis of myofiber composition reveals muscle-specific disease and age-associated patterns. FASEB J. 2019;33:4046–53.

17. Riaz M, Raz Y, Moloney EB, van Putten M, Krom YD, van der Maarel SM, et al. Differential myofiber-type transduction preference of adeno-associated virus serotypes 6 and 9. Skeletal Muscle. 2015;5:37–7.

18. Riaz M, Raz Y, van Putten M, Paniagua-Soriano G, Krom YD, Florea BI, et al. PABPN1-dependent mRNA processing induces muscle wasting. PLoS Genet. 2016;12:e1006031.

19. Komiya Y, Sawano S, Mashima D, Ichitsubo R, Nakamura M, Tatsumi R, et al. Mouse soleus (slow) muscle shows greater intramyocellular lipid droplet accumulation than EDL (fast) muscle: fiber type-specific analysis. J Muscle Res Cell Motil. 2017;38:163–73.

20. Van Leeuwen JL, Spoor CW. Modelling mechanically stable muscle architectures. Proc R Soc London, Ser B. 1992;336:275–92.

21. Moo EK, Fortuna R, Sibole S, Abusara Z, Herzog W. In vivo sarcomere lengths and sarcomere elongations are not uniform across an intact muscle. Front Physiol. 2016;7:1–9.

22. Moo EK, Leonard TR, Herzog W. The sarcomere force-length relationship in an intact muscle-tendon unit. J Exp Biol. 2020;223:1–9. https://doi.org/10.1242/jeb.215020

23. Mathewson MA, Chapman MA, Hentzen ER, Fridén J, Lieber RL. Anatomical, architectural, and biochemical diversity of the murine forelimb muscles. J Anat. 2012;221:443–51.

24. Damon BM, Buck AKW, Ding Z. Diffusion-tensor MRI based skeletal muscle fiber tracking. Imaging Med. 2011;3:675–87.

25. Sullivan SP, McGechie FR, Middleton KM, Holliday CM. 3D muscle architecture of the pectoral muscles of European Starling (Sturnus vulgaris). Integr Organismal Biol. 2019;1:1–18. https://doi.org/10.1093/iob/oby010

26. Lowe DG. Distinctive image features from scale-invariant Keypoints. Int J Comput Vision. 2004;60:91–110. https://doi.org/10.1023/b:visi.0000029664.99615.94

27. Heemskerk AM, Strijkers GJ, Vilanova A, Drost MR, Nicolay K. Determination of mouse skeletal muscle architecture using three-dimensional diffusion tensor imaging. Magn Reson Med. 2005;53:1333–40. https://doi.org/10.1002/mrm.20476

28. Tse N, Morsch M, Ghazanfari N, Cole L, Visvanathan A, Leamey C, et al. The neuromuscular junction: measuring synapse size, fragmentation and changes in synaptic protein density using confocal fluorescence microscopy. J Visualized Exp. 2014;52220. https://doi.org/10.3791/52220

29. Herzog W. Skeletal muscle mechanics: questions, problems and possible solutions. J Neuroeng Rehabil. 2017;14:98.

30. Stark H, Schilling N. A novel method of studying fascicle architecture in relaxed and contracted muscles. J Biomech. 2010;43:2897–903. https://doi.org/10.1016/j.jbiomech.2010.07.031

31. Dickinson E, Stark H, Kupczik K. Non-destructive determination of muscle architectural variables through the use of DiceCT. Anat Rec (Hoboken). 2018;301:363–77.

32. Nyakatura JA, Baumgarten R, Baum D, Stark H, Youlatos D. Muscle internal structure revealed by contrast-enhanced μCT and fibre recognition: the hindlimb extensors of an arboreal and a fossorial squirrel. Mamm Biol. 2019;99:71–80.

33. Lovering RM, Shah SB, Pratt SJP, Gong W, Chen Y. Architecture of healthy and dystrophic muscles detected by optical coherence tomography. Muscle Nerve. 2013;47:588–90. https://doi.org/10.1002/mus.23711

34. Wang L, Copray S, Brouwer N, Meek MF, Kernell D. Regional distribution of slow-twitch muscle fibers after reinnervation in adult rat hindlimb muscles. Muscle Nerve. 2002;25:805–15. http://dx.doi.org/10.1002/mus.10114

35. van Leeuwen JL, Spoor CW. A two dimensional model for the prediction of muscle shape and intramuscular pressure. Eur J Morphol. 1996;34:25–30. https://doi.org/10.1076/ejom.34.1.25.13155

36. Lomo T. What controls the position, number, size, and distribution of neuromuscular junctions on rat muscle fibers? J Neurocytol. 2003;32:835–48.

SUPPORTING INFORMATION

Additional supporting information may be found online in the Supporting Information section at the end of this article.